

Full length article

Assessment of residual stress fields at deformation twin tips and the surrounding environments



Hamidreza Abdolvand*, Angus J. Wilkinson

Department of Materials, University of Oxford, Parks Road, Oxford OX1 3PH, UK

ARTICLE INFO

Article history:

Received 16 October 2015

Accepted 20 November 2015

Available online 30 December 2015

Keywords:

Twin

Localized deformation

HR-EBSD

Twin intersections

ABSTRACT

Stress fields close to twin tips and the associated local neighbourhoods of a hexagonal close-packed (HCP) polycrystal were studied in detail. For this purpose, a coarse grain textured Zircaloy-2 sample was firstly strained uniaxially in a macroscopic direction that favours tensile twin formation. The sample was then unloaded and residual elastic strains and lattice rotations measured using the high-resolution electron backscatter diffraction (HR-EBSD) technique. Measured elastic strain maps of various clusters of grains including parent and twin pairs were then analysed. Stress, dislocation density, and their associated concentrations close to twin tips, within twins, in the immediate neighbouring grain, at the intersection of two twins, and within parent grains were investigated. It is shown that the stress field at the twin tips varies as a function of local neighbourhood. High stress, lattice rotation, and dislocation density concentrations were generally observed close to twin tips both within twins and within the immediate neighbouring grains. It is shown that dislocation density concentration is maximum at the intersection of two twins which can potentially provide susceptible site for crack nucleation.

© 2015 Acta Materialia Inc. Published by Elsevier Ltd. This is an open access article under the CC BY license (<http://creativecommons.org/licenses/by/4.0/>).

1. Introduction

Due to a lack of easy slip system availability, deformation along the c-axis of HCP crystals is often accommodated by a swift change in the orientation of portion of the grain, in a process known as twinning. Nucleation, propagation, and thickening are three stages associated with twin formation. As a result of being swift, at least during nucleation and propagation, capturing load partitioning between parent and twin experimentally has remained nontrivial. The significance of understanding such localized stress field is in determining their associated effects either on accommodating deformation close to crack tips or on nucleation and propagation of cracks and thus their tendency to limit ductility. For instance, the effects of microstructural factors in formation of twins at the crack tip of a wrought magnesium alloy during fracture toughness tests was studied by Somekawa et al. [1]. It was shown that stress concentration at the crack tip facilitates twin formation, however twinning was suppressed when the grain size was refined. A similar study by Wang et al. [2] has shown in Mg that under non-proportional biaxial tensile test, deformation twins play

significant role at the crack tip, however due to lower stress concentration associated with equiaxial tension, deformation by basal slip becomes the major deformation mode. Although these two studies provide significant insight into understanding interaction between twins and cracks, the localized stress fields, particularly at the grain-scale level were missing. Similar to HCP polycrystals, deformation twinning is believed to be a characteristic deformation mode in low stacking fault energy face-centred cubic (FCC) polycrystals. A significant contribution to understand the effect of twins on crack nucleation in such materials was given by Müllner et al. [3], where it was shown that stress fields associated with two intersecting twins can cause crack nucleation which eventually result in brittle fracture in austenitic steels with high manganese and nitrogen content. Recent observation has also confirmed the effect of stress field at twin tips in hydrogen-assisted cracking of twinning induced plasticity (TWIP) steels [4]. Interestingly, while it was found that intersection of twins with grain boundaries can act as crack nucleation sites, cracks can propagate along both non-coherent grain boundaries and deformation twin boundaries depending on the deformation twin alignment with respect to the loading direction. This observation is in agreement with the recent numerical study of crack nucleation in ultrafine-grained materials where it was shown that the angle that a twin boundary makes with the boundary of the neighbouring grain plays a role in crack

* Corresponding author.

E-mail addresses: hamidreza.abdolvand@materials.ox.ac.uk, hamid.abdolvand@gmail.com (H. Abdolvand).

nucleation [5]. Stoll and Wilkinson have used dislocation boundary element modelling to study the influence of pre-existing deformation twins on cracks passing close to twin tips and their results suggest that local residual stresses near deformation twin bands could contribute to intergranular stress corrosion cracking in cold worked stainless steels [6]. Studies on the effects of annealing twins in nickel based superalloys show that most cracks were effectively coincident with coherent twin boundaries [7] and preferred high cycle fatigue crack initiation correlate strongly with the trace length of the longest twins. Elastic anisotropy and the resulting compatibility stresses are believed to be the driving force for the localisation of plasticity and subsequent crack formation as established in Cu by Heinz & Neumann [4]. Further, the effects of deformation twins in failure of nickel based single crystal superalloys during thermomechanical fatigue loading was studied by Sun et al. [8,9]. It was shown that deformation twins cause crack formation close to the sample surface and cracks then propagate along the twin boundaries. This twinning and crack formation is often linked to micropores located close to crack tip. These experimental observations on the role of twins in crack nucleation and propagation, make clear that further understanding of stress distribution around twin tips is required.

Various diffraction based techniques have been used to study stress levels during deformation twinning. For example in-situ neutron diffraction experiments on MgAZ31 [10] and Zircaloy-2 [11] have indicated that the newly formed twins are relaxed comparing to their parent grains. While lattice strain measurement with neutron diffraction technique normally provides an excellent statistical representation of the bulk [12,13], as a result of averaging, local elastic-strain fields associated with individual twin will be missed. The evolution of average stress over entire twin and parent pairs has been studied using three-dimensional synchrotron x-ray diffraction [14–18]. In these studies it is shown that the stress normal to the twin habit plane within twin and parent are same. This technique provides the average elastic strain within an individual grain but still the spatial distribution of stress field within each grain is missing. Differential-aperture X-ray microscopy has been used to study such spatial variation of stress field within a twinned grain of MgAZ31 alloy [19] and it was reported that there is high elastic strain gradient close to the twin boundary. Although this technique provides the full stress tensor in bulk materials, statistical analysis of twins would be costly due to time constraints and so results are currently limited to observations on a single twin.

High resolution electron backscatter diffraction (HR-EBSD) is another diffraction-based technique that can be used for measuring stress variations at high spatial resolution at sample surface. With this method, elastic strain variations and lattice rotations can be calculated based on the shifts in features of Kikuchi diffraction patterns collected for deformed and undeformed samples [20,21]. With this technique deviatoric stress can be extracted directly, however to calculate the hydrostatic stress an extra equation is required. It is feasible to calculate the hydrostatic stress by using the knowledge that surface normal stress is zero as measurements are carried out at the sample surface. With this the whole stress tensor can be determined [22]. It is shown that with using image based cross-correlation, pattern shifts can be measured with sub-pixel precision with subsequent precision of 10^{-4} in elastic strain and 10^{-4} rad in lattice rotation measurements [22], or even better if pattern averaging is employed [23]. With this technique, it is feasible to measure stress variation within each grain with spatial resolution as small as 18 nm close to grain boundaries [24]. Since there is a lot of freedom in moving the electron beam over the sample area at different step sizes the technique is very flexible and can either target specific local features or be used over wider areas for statistical analysis.

Although stress concentration close to twin tips can be detrimental and can diminish the life span of components, they are not well characterized. In this study, as a step toward achieving such a goal, the state of deformation close to twin tips and their neighbourhoods in a deformed Zircaloy-2 sample are studied in detail. The HR-EBSD technique is used to measure orientation, grain shape, relative elastic strain and lattice rotation, and geometrically necessary dislocation (GND) density close to various deformation twins and their associated neighbourhoods. Stress fields associated with some twins are subsequently characterized, attention is particularly given to the stress concentration in the environment surrounding the twin.

2. Sample preparation and measurement set up

The material used was Zircaloy-2 taken from a textured warm rolled slab. This material has been well-characterized with in-situ neutron diffraction [25], EBSD [26,27], and finite element modelling [28]. The slab is α -zirconium with HCP crystal structure at room temperature and with nominal composition Zr, 1.2–1.7 wt% Sn, 0.07–0.2 wt% Fe, 0.05–0.15 wt% Cr, 0.03–0.08 wt% Ni, 1400 ppm oxygen [29]. A previous texture measurement on the slab indicated that most of the basal plane normals are oriented toward the Normal Direction (ND). This material was then heat treated and mechanically loaded in several cycles to grow the average grain size to $\sim 50 \mu\text{m}$. EBSD analysis of this material had indicated that the misorientation between the c-axis of the HCP crystal and the ND direction is less than 30° in more than 62% of grains. A dog-bone sample was subsequently made with gauge length of 10 mm and cross section of $1 \times 1 \text{ mm}^2$. This sample was then uniaxially strained in a macroscopic direction that favours twinning up to a tensile strain of 2.7% ($\sigma = 450 \text{ MPa}$) with strain rate of $\dot{\epsilon} = 5 \times 10^{-5} \text{ s}^{-1}$. The sample was polished after unmounting from the tensile stage. Mechanical polishing was conducted using various grades of silicon carbide paper down to 4000 grit followed by polishing in 50 nm colloidal silica suspension for about two hours. At this stage it was not yet possible to collect high quality Kikuchi patterns, hence the sample was Ar ion polished with a PECS-II (<http://www.gatan.com/products/sem-specimen-preparation/pecs-ii-system>) using 7.5 keV beam energy under dual beam condition, with gun angle of 8° and for about 15 min. This setting resulted in collection of high-quality Kikuchi patterns. An EBSD map of deformed sample with two example of Kikuchi patterns acquired, one in a middle of a grain and one close to twin boundary, are shown in Fig. 1. Although generally a high GND density is calculated close to twin tips (see Section 3 and 4) the ion polishing resulted in capturing excellent patterns that facilitate cross-correlation even at the highly deformed areas.

Data collection was carried out in a Zeiss MERLIN Field Emission Gun Scanning Electron Microscope (FEG-SEM) with 20 keV beam energy, 15 nA current, and working distance of 18 mm. Kikuchi patterns were collected using a high resolution EBSD detector made by Bruker system. For each scanned area the EBSD detector was set at about 17.5 mm distance from the sample surface where this distance was calibrated using 30 patterns collected over the entire scanned area. At each scanned point, an 800×600 pixels Kikuchi pattern was collected with exposure time of 180 ms per pattern with no gain applied. These settings provide reasonable collection time for measuring an entire map while providing accurate estimation of GND densities [30,31]. For each collected map different step size was used and these are stated in Section 3.

Elastic strain and lattice rotations are calculated by cross-correlation analysis of the collected Kikuchi patterns. In order to enhance the quality of cross correlation results, each pattern was firstly divided into 40 square sub-regions, also called Region of

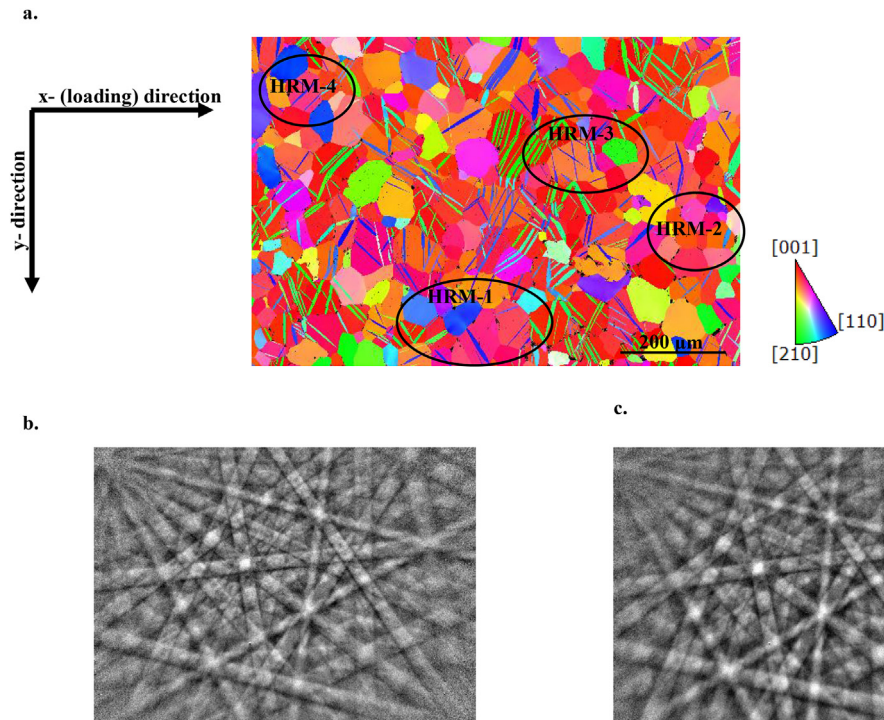


Fig. 1. (a) an EBSD map of the deformed sample indicating the areas that HR-EBSDs are performed. Grains are colour coded with respect to the loading direction (x-axis) with red colour indicating c-axis of HCP crystal pointing toward loading direction. (b) An example of Kikuchi pattern acquired in the middle of the grain M2G2 (see also Fig. 3a) and used as a reference pattern. (c) Kikuchi pattern from the same grain but located at the shared grain boundary with M2T6.

Interest (ROI), which consist of 128×128 pixels. These ROIs were selected in such a way that the first one was located in the middle of the Kikuchi pattern with 19 others located with equal distance on the perimeter of a circle centred on the first ROI. Random positions were assigned to the other 20 ROIs. After transforming each ROI into Fourier domain, high pass and low pass filters were applied to remove background and noise, respectively. Since the sample was deformed and each grain has residual stress, it was not possible to acquire Kikuchi pattern from stress free regions. Hence, for each grain a reference point was selected as a position well away from grain boundaries and showing low kernel average misorientation where it was possible to acquire a high quality Kikuchi pattern. By cross-correlating Kikuchi patterns acquired at other points within the grain and the corresponding reference point, it is possible to calculate pattern shifts; with assuming that the stress normal to surface is zero, relative elastic strains and lattice rotations can subsequently be calculated [22]. The measurement of absolute elastic strain and lattice rotation with this method is the subject of ongoing research [32].

Since lattice rotations can be large particularly close to twin tips or grain boundaries, the remapping method developed in Ref. [33] was used to calculate deformation gradients. Elastic strains are typically limited to up to $\sim 0.2\%$ which result in shifts at the pattern centre of up to 2 pixels [21] however this movement can be overshadowed by large lattice rotations particularly when they exceed $\sim 1^\circ$ rotation which cause pattern shifts of several tens of pixels [34] (see for example Fig. 1b and c). To solve this problem, the first pass of cross-correlation was used to calculate elastic strains and lattice rotations. These rotations were then used to remap the test pattern intensities into the reference pattern orientation and use a second pass of cross-correlation from which elastic strains and corrections to lattice rotations are calculated. The deformation gradient from the first and the second pass are subsequently combined to determine the total deformation gradient and hence to calculate the

Green strain tensor. The measured elastic strains are then used to calculate residual stress tensor using elastic modulus of pure zirconium: $C_{11} = 143.5$ GPa, $C_{33} = 164.9$ GPa, $C_{12} = 72.5$ GPa, $C_{13} = 65.4$ GPa, and $C_{44} = 32.1$ GPa [35]. It is worth mentioning that it is reasonable to use elastic modulus of pure zirconium for this case as Zircaloy-2 is a dilute solution of zirconium.

Once lattice rotations are determined, it is possible to calculate the GND density using the spatial gradient of lattice rotation and Nye's dislocation tensor [36]. Since it is not possible to calculate rotation gradient through the thickness with HR-EBSD, just six out of nine components of rotation gradient tensor can be calculated. These component are then used to estimate the GND density stored in each grain assuming that there are three a screw, three a edge on basal, three a edge on prism, six a edge on pyramidal, six $c + a$ screw, and twelve $c + a$ edge on pyramidal, dislocation types. Since, the six lattice rotation gradients do not provide enough information to calculate dislocation density on each of the 33 dislocation types unambiguously, a lower bound GND density is estimated by minimizing the possible total line energy [37] while meeting the 6 measured lattice curvature constraints. This method provides one answer of many possible ones. Modification of this technique is the subject of ongoing research. It is worth mentioning that the calculation of GND densities with this method is not affected by the state of the reference point as the gradients of rotation are used.

3. Results

An analysis of interaction between many twins and their corresponding neighbourhoods is given in this section. In order to provide statistical information regarding the state of the Zircaloy-2 sample, an EBSD map of the deformed-unloaded sample that was measured over an area of $1 \times 0.6 \text{ mm}^2$ is shown in Fig. 1a. All of the so-called inverse pole figure maps shown in this paper are coloured with respect to the crystal direction along the horizontal x-axis

which corresponds to the loading direction. It is clear from Fig. 1a that most of the parent grains have their crystal c-axis oriented close to the loading direction which has encouraged many twins to form. In some grains more than five twins of the same variants are formed whereas in some others there are more than two active twin variants. This facilitates categorizing twin interactions into four groups: (a) interaction of twins with their immediate neighbouring grain, (b) twin–twin interaction, (c) twin–parent interaction, and (d) state of the twin itself. These interactions are studied in detail by running HR-EBSD on four different areas. These are named as HRM which represent High-Resolution Map that follows with a number. These areas are indicated in Fig. 1a and the set up used for measurement is given in Table 1.

The HR-EBSD maps of these areas are shown in Figs. 2–5. The reason why these particular areas are selected to study is that they provide a good combination of interaction of twins with both hard and soft immediate neighbouring grains. In what follows general trends observed in the measured maps are discussed within the framework of the four categories identified above. The layout of Figs. 2–5 is the same with the top row giving an inverse pole figure map in which significant parent grains and twins are labelled, an image quality map on which positions of all the reference points used are marked, and a GND density map. The second row shows the variation from the reference stress state within each grain for the three in-plane stress terms (σ_{11} , σ_{22} , and σ_{12}), and the final row shows the lattice rotations about the three macroscopic Cartesian axes (ω_{12} , ω_{13} , and ω_{23}).

Grains and twins described and discussed in the paper are identified using ID codes which start with an M and a number representing the HRM map number followed by G or T representing either Grain or Twin, and then a final digit is for distinguishing between different grains. For instance, M1G1 represent grain no. 1 in map HRM-1 while M2T6 represent twin no.6 in map HRM-2.

It is also worth mentioning that at room temperature $\{10\bar{1}2\} \langle \bar{1}011 \rangle$ tensile twin are the dominant twin system. This tensile twin system results in approximately 85° misorientation between basal plane normal within twin and that of parent. Also, the twin shear associated with twin formation is 0.169. In what follows the six variants of the tensile twins are named as variant-1, variant-2, variant-3, variant-4, variant-5, variant-6 that represent $(10\bar{1}2)[\bar{1}011]$, $(01\bar{1}2)[0\bar{1}11]$, $(\bar{1}102)[1\bar{1}01]$, $(\bar{1}012)[10\bar{1}1]$, $(0\bar{1}12)[01\bar{1}1]$, $(1\bar{1}02)[\bar{1}101]$, respectively.

In Fig. 2b–5b, the reference points picked for calculating relative elastic strain for each grain are illustrated with a cross. The quality of patterns collected are characterized by a number ranged between 12 and 0 representing high quality and low quality pattern, respectively. This indicate that in HRM-1 to HRM-4, the quality of Kikuchi patterns acquired for most of the probed points is higher than 8 which is suitable for cross-correlating patterns. This reflects the ability of PECS-II for preparing good surface-finish samples that high quality Kikuchi patterns can be acquired from. As mentioned above, having high quality Kikuchi patterns is an essential for the implemented cross-correlating technique.

3.1. Twin-neighbouring grain interaction

Maps HRM-1 and HRM-2 provide information regarding interaction between various twins and neighbour and parent in grains in both soft and hard orientations with respect to the external loading. The measured orientation of each grain along with the misorientation between the basal plane normal and the loading direction, the maximum global Schmid factor of prism, basal, pyramidal $c+a$, and tensile twinning system are provided in Appendix A in table A1.

In Fig. 2c, the spatial distribution of GND density is illustrated. Colours are coded in the \log_{10} scale and represent number of dislocations per unit area (m^{-2}). The average GND density measured for this map is $6.86 \times 10^{13} \text{ m}^{-2}$ though higher density is observed both at the grain boundaries and twin tips. The GND density of M1G1 is generally higher than most of the grains since (a) prism slip system is well aligned for accommodating the externally applied strain (see table A1), and hence is highly active, (b) it is surrounded by many hard grains so that both a high strain and high strain gradient need to be accommodated in this grain, and (c) the relatively large twins M1T5 and M1T6 impinge on its boundaries toward the lower end where the GND density is greatest. In contrast to M1G1, both M1G4 and M1G7 have their c-axis relatively aligned with the loading direction and hence have high pyramidal slip and tensile twinning activity. That is why M1G4 is twinned. Both of these two grains have an intersection with twins, M1T1 and M1T2, but the GND density close to the twin tips within these grains are much lower than in M1G1 reflecting that not much of deformation from the twin formation is accommodated within them.

In Fig. 3c, the calculated GND density for map HRM-2 is shown. The average dislocation density measured in this map is $8.81 \times 10^{13} \text{ m}^{-2}$ which is ~28% higher than that calculated for HRM-1. This is compatible with orientation maps as there are more soft grains within HRM-2 than within HRM-1, but it should also be noted that a smaller step size was used for HRM-2 (see Table 1) and so GNDs may make a greater fraction of the total dislocation density. M2T6, is much thicker in comparison to many other twins presented in HRM-1 and HRM-2 and has a blunt tip in south and even wider open tip in the north. The dislocation density measured ahead of the open tip within M2G2 is higher than that in M2G7 ahead of the blunt tip of this twin. The extent of dislocation concentration is also much higher within M2G2 than M2G7 reflecting the effect of twin tip and twin propagation on the accommodation of plastic deformation in the neighbouring grain. It is worth mentioning that in the presented maps, for the areas where there is high uncertainty in the quality of cross-correlation, results are replaced with white colour (M2T5 for instance).

In Fig. 2d–f, measured relative stresses for HRM-1 are illustrated. EBSD is a near surface technique and so stresses acting across the sample surface σ_{13} , σ_{23} , and σ_{33} are expected to be small and so are not shown in Figs. 2–5 (indeed σ_{33} is explicitly set to zero in calculating the hydrostatic strain). Also, the elastic lattice rotations are shown in Fig. 2g–i. From Fig. 2d–i, it can be concluded that generally there appear to be higher stress and lattice rotation concentration in the twin's neighbouring grain. It is generally

Table 1
HREBSD setup for the four maps studied here.

Region	Figure	No of points	Step size (nm)	Detector distance (mm)	Interaction types ^a
HRM1	2	512 × 384	441	18.09	T–N, T–P
HRM2	3	580 × 435	278	18.06	T–N, T–P
HRM3	4	512 × 384	276	16.98	T–T
HRM4	5	550 × 412	316	17.01	T–T, T–P

^a T, N, and P represent Twin, Neighbour, and Parent grains.

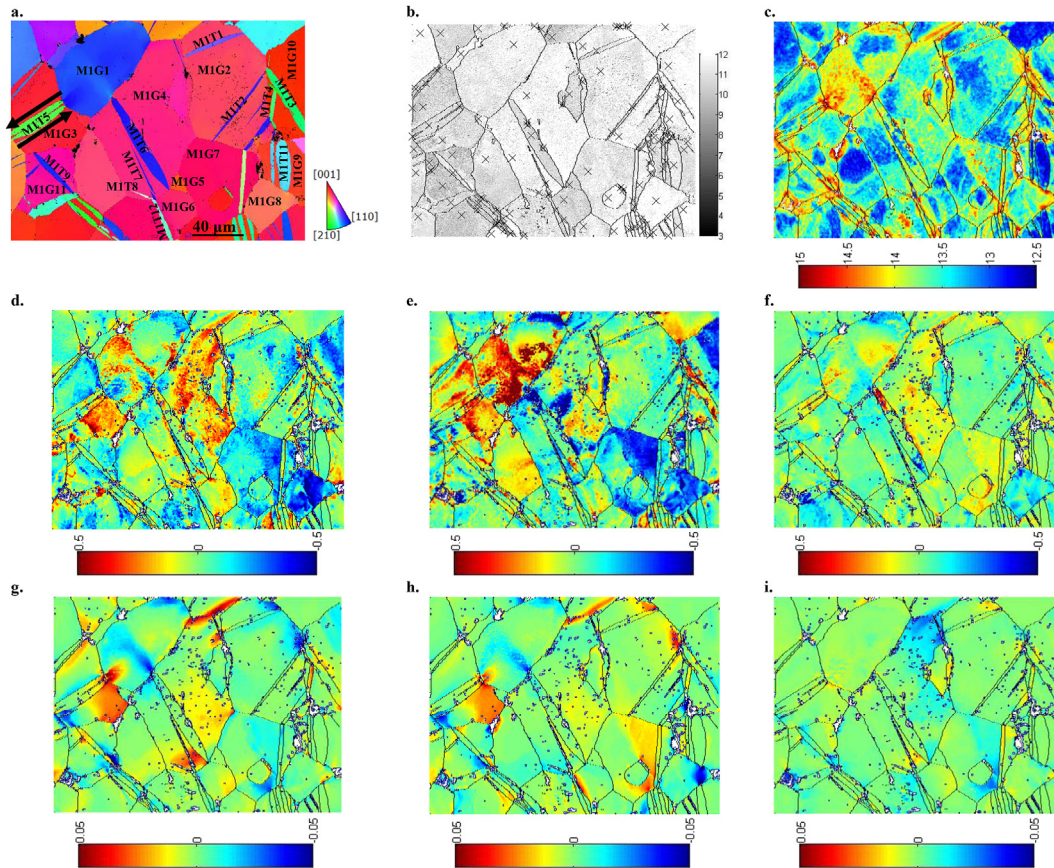


Fig. 2. (a) High resolution EBSD map of HRM-1 with IDs assigned to each grain and twin. (b) a map of quality of each pattern acquired with crosses indicating reference points used for relative stress calculation. Maps of (c) GND density, (d) stress σ_{11} , (e) σ_{22} , (f) σ_{12} , (g) elastic lattice rotation ω_{12} , (h) ω_{13} , (i) ω_{23} . Scale bar for each series is indicated under the figure where GND density, stresses, and rotations are given in Log10 scale (m⁻²), GPa, and radians, respectively.

believed that the shear stress required for twin nucleation is higher than that required for its thickening. Hence, twin nucleation and propagation involves an overshoot in the shear required to accommodate the applied deformation. This process results in a back stress within the twin and stress concentration in the neighbouring grain which can cause plastic slip or in some cases even result in nucleation of another twin within the neighbouring grain [10,38]. For instance, a high stress and rotation concentration can be observed in σ_{22} , σ_{12} , ω_{12} , and ω_{13} components in M1G1 close to its intersection with M1T5. To shed more light on this, with orientation analysis of M1T5 and the associated parent grain M1G3, it can be concluded that the specific twin variant formed was $(1\ 0\ \bar{1}\ 2)\ [\bar{1}\ 0\ 1\ 1]$. Twin trace analysis also confirms this calculation although it was shown that twin plane can sometimes deviate significantly from the theoretical one calculated from the parent's orientation [39]. The direction of the twin shear associated with M1T5 in the x-y plane of the map is shown in Fig. 2a. The twin shear mandates that the resulting rotation field in the neighbouring grain about z axis (ω_{12}) should be positive close to M1T5 tip. This is compatible with what is measured and presented in Fig. 2g.

Stress distribution and lattice rotation variations within each grain for HRM-2 are shown Fig. 3d to i. These maps follow the similar trends as discussed for features in HRM-1. For instance, there is a high rotation concentration close to the M2T6 tip within M2G2. The orientation analysis of this twin and parent grain indicates that the $(0\ 1\ \bar{1}\ 2)\ [0\ \bar{1}\ 1\ 1]$ twin variant formed with the twinning shear direction as shown in Fig. 3a. This shear direction should induce a positive lattice rotation in neighbouring grain M2G2 which is compatible with what was measured in Fig. 3g.

Similarly a high stress concentration in all of the stress components is captured close to M2T6 tip within M2G2.

3.2. Twin–twin interaction

As stated in section 1, different studies have reported twin intersections as the potential sites for crack nucleation [3]. To understand the possible reason, in this section twin–twin interactions are studied. Several twin intersections are observed in the HR-EBSD maps HRM-3 and HRM-4 (Figs. 4 and 5).

Two twin variants are active in the grain M3G1 where they intersect at the middle of the parent grain. The reference points selected to study M3T1 and M3T2 are far from the intersection in case there is a stress concentration, it can be captured. Both the GND and stress maps indicate that there are higher concentrations close to the intersection point. Deformation and rotation at the intersection are so high that the cross correlation technique was not successful to calculate variations across the whole area of intersection. Nevertheless, concentrations are significantly high within the twins, for instance in case of σ_{11} and σ_{22} , GND. The same trend is also observed for the intersection of M3T9 with M3T10, M3T6 with M3T5, and M4T2 with M4T1.

In other cases the twin interaction is across a grain boundary between two parent grains, for instance, the interaction of M3T4 with M3T5 or M4T4 with M4T3. As the experiment was performed ex-situ it is difficult to comment as to whether one of the twins in any of these pairs resulted in nucleation of the other twin. Nevertheless, in both cases high dislocation density and stress concentration are observed at the tip of the twins.

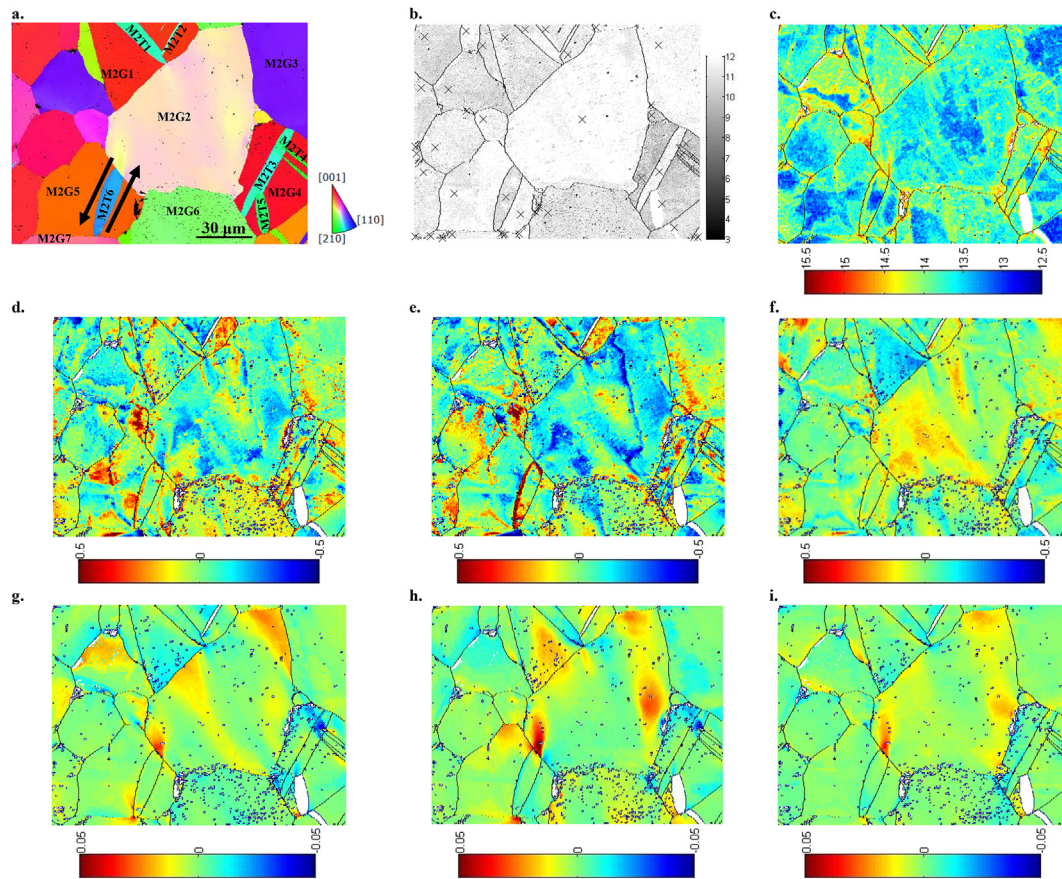


Fig. 3. (a) High resolution EBSD map of HRM-2 with IDs assigned to each grain and twin. (b) a map of quality of each pattern acquired with crosses indicating reference points used for relative stress calculation. Maps of (c) GND density, (d) stress σ_{11} , (e) σ_{22} , (f) σ_{12} , (g) elastic lattice rotation ω_{12} , (h) ω_{13} , (i) ω_{23} . Scale bar for each series is indicated under the figure where GND density, stresses, and rotations are given in Log10 scale (m⁻²), GPa, and radians, respectively.

3.3. Twin-parent interaction and the state of deformation within twins

Analysis of results has shown that there are two classes of twin-parent interaction. For the first one, the twin is at the early stage of propagation, is not fully developed, and is fully embedded in the parent grain, e.g. M1T7, M1T8, and M4T6. For the second one, the twins are fully propagated and are at the thickening stage. Investigation of the maps acquired for the first case indicate that there is generally a high concentration of GND density at the twin-parent boundaries. This is followed by a high stress concentration in various stress components, particularly at the twin tips. In order to understand the rotation field close to these twins, as an example, analysis of variant selection was performed on M4T6–M4G5 pair. Variant analysis indicated that M4T6 is the twin variant $(\bar{1} \ 1 \ 0 \ 2) [1 \ \bar{1} \ 0 \ 1]$. The resulting simple shear is indicated by arrows in Fig. 5a. This twin shear induces a negative rotation about the z-axis (ω_{12}) which is captured in the HR-EBSD measurements (Fig. 5g). The resulting rotation calculated for this twin changes from the north surface of the twin to the south one, but on average it generates -1.26° rotation about the z-axis.

For the second group where twins have fully propagated and are at the thickening stage, analysis of different twin and parent pairs revealed that there is not a unique trend that can be specified for all of them. For instance, while there is high stress concentration and GND density within M2T6–M2G5, this is not the case for M1T11–M1G9. Nevertheless, each twin-parent pair has some areas close

to their boundary with higher concentration of stress and/or GND density associated with it.

Different twins are analysed to understand the state of the deformation inside each twin. Similar to the previous section, this state changes from the edge of the twin plate toward the tips, however, it can be seen that in most of the twins, there is a high concentration close to the twin tips. For instance, there is a high concentration in most of the stress components of M1T6, at both ends. Interestingly, the sign of the σ_{12} changes from the lower tip toward the north.

4. Discussion

Results presented in Figs. 2–5 indicate that generally there are stress, GND density, and lattice rotation concentration close to the twin tips both inside the twins and in their surrounding neighbourhoods. This is pronounced close to the twin boundaries and twin tips. A detailed discussion on the trends explained in section 3 is given here. Various parameters that can potentially affect the observed trends are given here. In what follows, $\Delta\theta_{Ba}$ represent the misorientation between basal plane normals of any two grains studied, TW_v represent the twin variant, and TW_{th} represent twin thickness at its widest point. One of the parameters that can affect stress concentration in the neighbouring grain is how well its slip systems are aligned to accommodate deformation generated by the twin. Different methods have been suggested as suitable misalignment parameters in considering slip transfer across grain

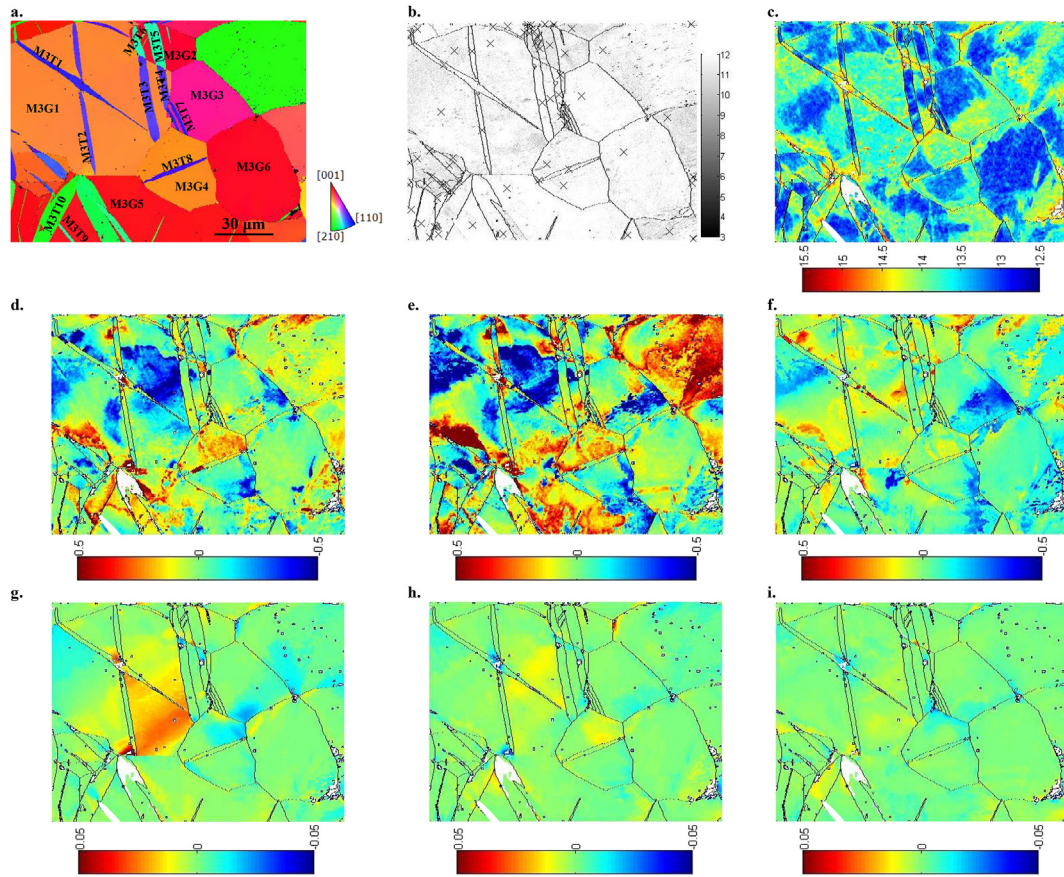


Fig. 4. (a) High resolution EBSD map of HRM-3 with IDs assigned to each grain and twin. (b) a map of quality of each pattern acquired with crosses indicating reference points used for relative stress calculation. Maps of (c) GND density, (d) stress σ_{11} , (e) σ_{22} , (f) σ_{12} , (g) elastic lattice rotation ω_{12} , (h) ω_{13} , (i) ω_{23} . Scale bar for each series is indicated under the figure where GND density, stresses, and rotations are given in Log10 scale (m⁻²), GPa, and radians, respectively.

boundaries [40,41], and here the one suggested by Werner and Prantl [42] is adapted by replacing the incoming slip plane normal with the twin habit plane normal \mathbf{n}_1 and the incoming Burgers vector with the twin shear direction \mathbf{b}_1

$$M = \frac{(\mathbf{n}_1 \cdot \mathbf{n}_2)(\mathbf{b}_1 \cdot \mathbf{b}_2)}{|\mathbf{b}_1||\mathbf{b}_2|} \quad (1)$$

where M is the alignment parameter that varies between 0 and 1, and \mathbf{n}_2 represent normal to the outgoing slip plane and \mathbf{b}_2 represents the outgoing slip direction. In this section, the alignment between the variant that caused twinning in the parent grain and the slip systems in the neighbouring grain is examined. Since each slip system has different variants, the maximum value of M calculated for all of the variants within the neighbouring grain are presented here. Hence, in what follows, $M_{TW-\alpha}$ represent the best alignment of twin in the parent grain with the slip system α in the neighbouring grain, where α can be basal, prism, or pyramidal $c+a$. Once the maximum M is determined, the Global Schmid factor of the aligned slip system in the neighbouring grains is calculated. This parameter is denoted S_α where α represent the slip system.

In all of the tables presented in this section results for the values measured in global coordinate (see Fig. 1) are given.

4.1. Twin-neighbouring grain interaction

In Section 3.1 we showed that there are stress and GND density concentrations close to the twin tips in the neighbouring grain, but

the magnitude of this concentration varies from twin to twin. Those parameters for some of the twin-neighbour pairs illustrated in Figs. 2–5 are quantified and presented in Table 2.

The extent of GND density and stress concentration changes from one case to another makes comparisons difficult. To unify the extent of the area that is used for measuring concentrations, we firstly plot a circle centred at the intersection of twin tip and neighbouring grain. Different radii can be used for this circle, but the one that we used is 1.5 times the maximum thickness of the intersecting twin (see Fig. 6a). The mean values of the stress and GND density for the set of points within this circle were calculated and are presented in Table 2. As an example, the extent of the areas in HRM-1 used for calculating concentrations are shown in Fig. 6a. A Concentration Factor (CF) is then defined to investigate the relative concentration of parameters with respect to the entire grain:

$$CF = \frac{\langle A \rangle_{\text{circle}}}{\langle A \rangle_{\text{entire grain}}} \quad (2)$$

where $\langle A \rangle_{\text{circle}}$ represent the value of the parameter (i.e. stress or GND density) measured at the twin tip within the neighbouring grain and $\langle A \rangle_{\text{entire grain}}$ represent the average value of the same parameter measured over the entire neighbouring grain.

It is worth mentioning that while the average value of GND does not depend on the selected reference point, the average value of stress, on other hand, does. Nonetheless, the reference points are selected to be in areas where the stresses are relatively uniform and

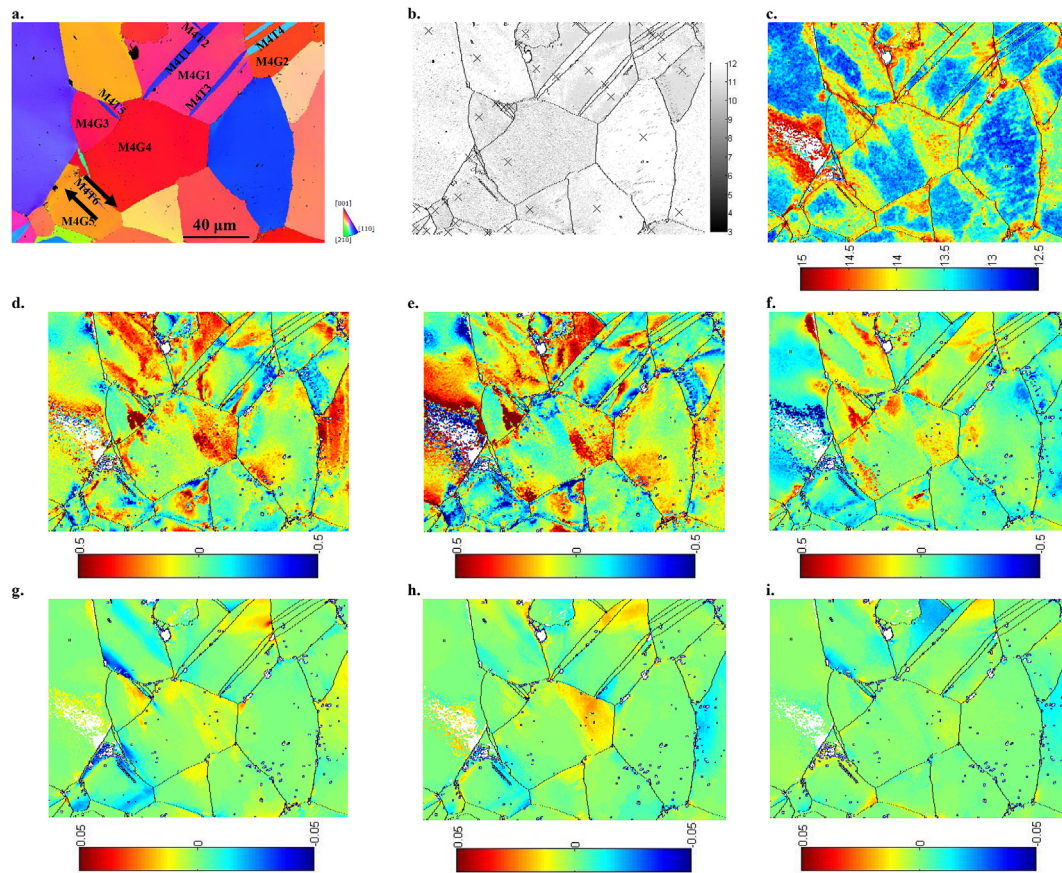


Fig. 5. (a) High resolution EBSD map of HRM-4 with IDs assigned to each grain and twin. (b) a map of quality of each pattern acquired with crosses indicating reference points used for relative stress calculation. Maps of (c) GND density, (d) stress σ_{11} , (e) σ_{22} , (f) σ_{12} , (g) elastic lattice rotation ω_{12} , (h) ω_{13} , (i) ω_{23} . Scale bar for each series is indicated under the figure where GND density, stresses, and rotations are given in Log₁₀ scale (m⁻²), GPa, and radians, respectively.

small comparing to the concentrated sites. Better determination of the CF values might be made by combining local HR-EBSD measurements with grain averaged stresses obtained from either 3D-XRD synchrotron experiments [16–19,43] or CP-FEA simulations [44]. In the current absence of such information reference points are placed in regions of low stress gradients in the hope that the absolute values of stress are also low there. A comprehensive study on the effects of varying the position of the reference point on the calculated stress is given in Ref. [45].

In section 3 it was shown that there is a higher GND density close to the tip of M1T6 within M1G1 and M1G6. In the Table 2 it is shown that, in comparison to M1G6, basal and prism systems in M1G1 are better aligned for accommodating the twin shear. This is the reason why both GND density and concentration factor are higher close to M1T6 tip within M1G1. Similarly, although M2T6 is a much thicker twin that interacts with a soft grain, due to not having a well aligned slip systems within M2G2, less GND density is induced at the opened end of M2T6. It is also worth to mention that, in this type of analysis the effect of the minimum driving force that requires for activating slip is neglected. For instance, critical resolved shear stress required for activating deformation by prism or basal is about three times less than that of pyramidal slip [46]. So, having pyramidal slip system aligned with the twin variant does not necessary mean that higher GND density will be calculated close to the twin tip within the neighbouring grain.

As an example of interaction of two twins of the same variant, the state of deformation at the intersection of M4T1 and M4T3 with M4G4 is presented in Table 2. It is shown that less GND density is induced within M4G4 at the intersection with M4T1 than its

intersection with M4T3, yet the reverse trend is observed for the state of stress and stress concentration factor. This may reflect the effect of the triple junction on the stress development close to M4T1 which result in completely different and complicated stress field.

Over all the twin-neighbour grain interactions assessed in the maps HRM1–4 shows that only a relatively weak correlation emerges between the best alignment of the easier slip systems (basal or prismatic for both Tables 1 and 2) and the concentration factor for GND density ahead of the twin tip. This is shown in Fig. 7a and b where GND densities and concentrations are plotted as a function of M_{TW-Ba} and M_{TW-Pr} . This suggests that although there is some correlation there are other factors that significantly moderate the interaction.

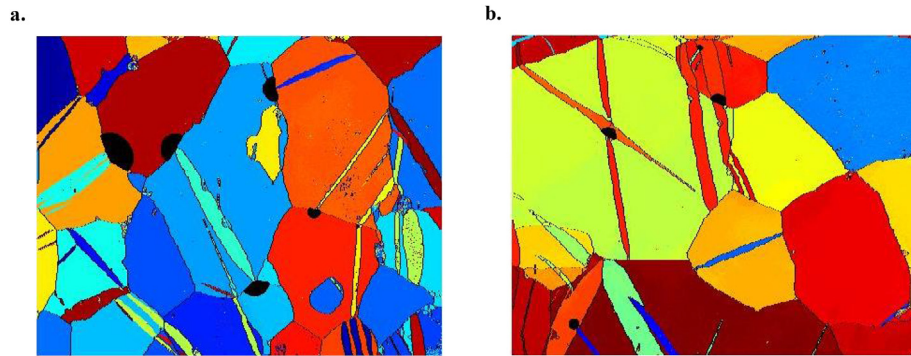
4.2. Twin–twin interaction

In section 3.2 we showed that there is stress and GND density concentration at the intersection of twins. The magnitude of such concentrations are measured and are presented in Table 3. Similar to section 4.1, the area that is used for calculating concentration are defined by a circle whose size is proportional to the twin thickness. However, since twins are thin, the circle is drawn with a radius 0.75 times the twin thickness in order to accommodate the circle within the twin. The data shown in Table 3 represent the concentrations that are induced in Twin-2 by intersecting Twin-1. As an example, the extent of the areas that are used for calculating concentration factors for twin–twin interactions in HRM-3 are shown in Fig. 6b.

Table 2

Quantitative analysis of interaction between twins and their associated immediate neighbour.

Twin	Neighbour	$\Delta\theta_{Ba}$ Deg.	TW_V	TW_{th} μm	M_{TW-Ba}	S_{Ba}	M_{TW-Pr}	S_{Pr}	M_{TW-Py}	S_{Py}	M_{TW-Tw}	S_{Tw}	GND (m^{-2})	σ_{11} GPa	σ_{22} GPa	σ_{12} GPa
HRM-1																
M1T6 CF ^a	M1G1	49.35	5	4.99	0.725	−0.102	0.013	−0.474	0.180	−0.359	0.439	−0.177	14.4367	−0.180	−0.010	−0.143
M1T6 CF	M1G6	59.11	5	4.99	0.014	0.333	0.014	−0.036	0.709	0.181	0.339	0.375	2.473	−6.02	−0.04	16.24
M1T5 CF	M1G1	75.08	1	8.11	0.503	0.013	0.635	−0.474	0.166	−0.301	0.168	−0.073	13.6944	0.134	−0.075	0.071
M1T1 CF	M1G4	41.32	4	3.74	0.138	−0.421	0.499	0.107	0.920	0.143	0.624	0.341	0.74	1.19	−2.10	2.66
M1T2 CF	M1G7	87.83	5	1.87	0.122	−0.307	0.003	−0.065	0.371	0.087	0.192	0.373	14.3838	−0.088	0.160	0.11
M1T11 ^a CF	M1G8	50.55	3	15.0	0.851	−0.475	0.092	−0.196	0.363	0.302	0.511	0.82	2.166	−2.93	0.74	−12.5
													14.1454	0.242	0.04	0.113
													2.33	1.64	−1.05	1.54
													14.1187	−0.192	−0.26	0.018
													1.91	1.08	1.53	0.51
													14.0635	−0.30	−0.29	−0.128
													1.33	1.20	1.2	1.02
HRM-2																
M2T6 CF	M2G2	89.0	2	5.90	0.290	−0.316	0.307	−0.181	0.12	0.056	1E-4	0.104	14.1967	−0.037	−0.109	0.091
M2T1 CF	M2G2	28.89	5	9.05	0.452	−0.116	0.052	0.362	0.791	0.019	0.860	0.123	2.22	0.944	1.05	1.56
M2T3 CF	M2G3	40.52	5	4.33	0.981	−0.017	0.157	0.039	0.337	−0.056	0.523	0.009	13.9162	−0.034	−0.120	0.033
M2T3 CF	M2G6	53.23	5	4.33	0.725	0.204	0.1306	−0.432	0.115	−0.370	0.359	0.051	1.16	0.857	1.16	0.556
													13.9878	0.022	0.058	0.116
													1.58	0.711	1.493	1.88
													14.0384	0.142	0.12	0.098
													1.29	1.52	−29.52	13.48
HRM-3																
M3T8 CF	M3G5	72.07	5	2.73	0.025	0.180	0.786	−0.008	0.613	0.284	0.349	0.480	14.507	0.262	0.031	0.086
M3T8 CF	M3G6	81.79	5	2.73	0.102	−0.182	0.871	−0.013	0.495	0.372	0.223	0.482	4.03	0.673	0.402	−1.352
													14.116	−0.006	0.058	−0.046
													2.27	−0.502	−26.66	0.612
HRM-4																
M4T1 CF	M4G4	85.20	3	4.47	0.355	−0.192	0.044	0.022	0.344	0.481	0.1845	0.454	14.0856	−0.009	−0.203	0.104
M4T3 CF	M4G4	85.13	3	1.77	0.348	−0.192	0.052	0.022	0.344	0.481	0.191	0.454	1.58	−0.08	−3.73	2.0
													14.2089	0.107	0.183	0.067
													2.08	1.047	3.35	1.29

Ba, Tw, Pr, and Py represent Basal, Twin, Prism, and Pyramidal $\langle c + a \rangle$ systems.^a CF represent Concentration Factor.**Fig. 6.** Maps of (a) HRM-1 and (b) HRM-3 with black dots representing the extent of the areas used for averaging parameters.

In comparison to twin-neighbour interaction where the average GND density of $1.37 \times 10^{14} m^{-2}$ with CF equal to 1.94 is measured, at the intersection of twins a higher GND density of $2.51 \times 10^{14} m^{-2}$ and corresponding CF of 2.2 are measured. Further, analysis of shear transfer and slip alignment has indicated that there is not much correlation between the M misalignment parameter and stress or GND concentration measured at different intersections.

One of the reason that might cause such trend is that, at twin–twin intersection when twins are not geometrically aligned, e.g. M3T1 and M3T2, regardless of how good slip systems are aligned for shear transfer, the mean free path of dislocations on various slip systems are limited due to lenticular shape of twin. This parameter is not included in the slip transfer equation suggested by Werner and Prantl [42] (Eq. (1)). Further, for the twins that are geometrically aligned, e.g. M3T4 and M3T5, there are not many

systems that can accommodate such shear transfer. As a result, the twin intersection normally comes with very high GND density as well as stress concentration which are also susceptible to crack nucleation.

4.3. State of deformation within twins

The magnitude of the stress and GND density concentrations at the twin tips within the twins are presented in Table 4. Similar to section 4.2, concentrations are measured in the area made by a circle whose radius is 0.75 times the twin thickness and centred at the twin tip. Since each twin has two tips, in this section the tips that points to the north and south are labelled as north tip and south tip, respectively. For instance, the tip of M1T6 at the intersection with M1G1 is called north tip while the one that intersect

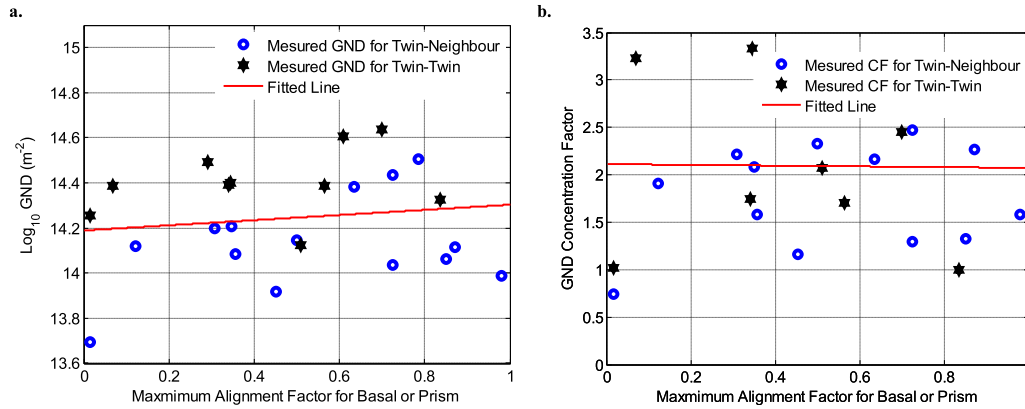


Fig. 7. (a) GND variation and (b) concentration as function of maximum alignment factor for prism and basal systems. Data are taken from both Tables 1 and 2.

Table 3
Quantitative analysis of interaction between intersecting twins.

Twin-1	Twin-2	$\Delta\theta_{Ba}$ Deg	TW_v	TW_{th} μm	M_{TW-Ba}	S_{Ba}	M_{TW-Pr}	S_{Pr}	M_{TW-Py}	S_{Py}	M_{TW-Tw}	S_{Tw}	GND(m^{-2})	σ_{11} GPa	σ_{22} Pa	σ_{12} GPa
HRM-1																
M1T3	M1T4	59.18	2	8.11	0.836	0.059	0.085	-0.476	0.081	-0.192	0.260	-9E-4	14.3241	0.0532	0.077	-0.078
CF													1.0	-1.143	-0.13	0.55
M1T3	M1T2	62.14	2	8.11	0.51	-0.155	0.121	-0.434	0.055	-0.065	0.188	-0.096	14.1241	0.0486	-0.258	0.061
CF													2.07	0.972	2.75	2.453
HRM-2																
M2T2	M2T1	10.65	2	1.97	0.341	-0.058	0.161	0.477	0.913	0.047	0.966	-0.077	14.3908	-0.214	-0.12	-0.29
CF													1.74	-14.28	-12.3	3.34
M2T5	M2T3	60.93	3	6.30	0.015	0.123	1.5E-5	-0.492	0.718	-0.482	0.449	-0.435	14.2565	0.127	-0.059	-0.105
CF													1.02	2.29	-4.18	1.435
M2T4	M2T3	60.00	3	1.57	0.70	-0.035	-0.033	-0.492	0.306	-0.362	0.423	-0.251	14.6362	0.33	0.45	-0.25
CF													2.456	5.93	32.66	3.47
HRM-3																
M3T2	M3T1	9.18	6	3.12	0.564	-0.008	0.144	0.054	0.778	-0.182	0.978	-0.082	14.3883	-0.736	-0.405	-0.511
CF													1.7	4.596	3.805	39.74
M3T6	M3T5	58.85	5	0.78	0.032	-0.057	0.068	-0.494	0.568	-0.064	0.266	-0.02	14.3879	0.255	-0.017	-0.022
CF													3.23	50.00	-1.166	-0.4762
M3T4	M3T5	29.50	4	3.12	0.345	-0.026	0.017	-0.494	0.914	-0.390	0.738	-0.273	14.3992	-0.205	-0.261	0.067
CF													3.33	-40.23	-17.52	14.33
M3T9	M3T10	61.02	4	1.56	0.092	0.116	0.610	-0.050	0.729	-0.452	0.496	-0.374	14.6057	0.315	-0.036	0.116
CF													NA	2.011	-0.709	1.87
HRM-4																
M4T4	M4T3	18.71	4	3.13	0.291	0.015	0.078	0.371	0.94	-0.079	0.914	-0.14	14.4933	0.009	-0.09	-0.023
CF													4.432	3.321	3.036	-0.797

M1G6 is called south tip.

The average GND measured for both side of twin tips and for all of the twins presented in Table 4 is $1.914 \times 10^{14} m^{-2}$ with average concentration factor of 2.15. This means that GND density in the twins near their tips is higher than in the neighbouring grain, yet it is less than those measured at the intersection of two twins. The state of deformation at each twin tip depends on the surrounding environment. For instance, in the case of M1T2 (north) and M1T9 (south) the GND density and stress concentrations are higher where the tip intersects another twin or a triple junction, respectively. This reflects the effect of tri-axial state of stress at the triple junction that affect state of stress within the twin.

In section 4.1 we showed that slip transfer from M1T6 to M1G1 is easier than slip transfer to M1G6 as slip systems in M1G6 are not so well aligned for such transfer. Compatible with this, the analysis of state of deformation at the north tip of M2T6 indicate that there is a very high concentration that might have been affected by the lack of shear transfer. The same trend is also observed for the state of deformation within M2T6 and its interaction with M2G2 and M2G7.

A statistical analysis of GND density variations close to twin tips

was undertaken leading to the plot in Fig. 8a in which the greyscale intensity indicates the frequency with which points at a given distance and at a given GND density level were found in the HR-EBSD map. Also shown on this are the 10%, 50% and 90% centile GND densities as a function of distance from the twin tip. There is a clear increase in the average GND density close to the crack tip. A function of the form $\log_{10}(\rho_{GND}) = A + B \exp(-Cx)$ was fitted to the data where 10^A represent the asymptotic value of the GND density, x represent the distance from the twin tip, and 10^B and C represent how strong and rapid the variation is close to the twin tip. No physical relevance is claimed for the function but it serves to capture the strength (through B) and length scale (through $1/C$) of the interaction. In Table 5 the value of A , B , and C for the four HRM-1:4 are presented. This analysis indicate that there is reasonable consistency from map to map on how on average the GND density increases close to the twin tips. Average values for A , B , and C across all four maps are 13.765, 0.783, 0.420, respectively for GND density in lines per m^2 and distance x in μm . $1/C$ indicates GND densities are significantly raised within 2.4 μm of the twin tip.

The stresses are a little more complicated due to their tensor nature, but can be reduced to a scalar field by considering the

Table 4

Quantitative analysis of deformation state within twins.

		TW_{th}	North tip				South tip			
		GND (m ⁻²)	σ_{11} GPa	σ_{22} GPa	σ_{12} GPa	GND (m ⁻²)	σ_{11} GPa	σ_{22} GPa	σ_{12} GPa	
HRM-2										
M1T6	4.99	14.0726	0.155	−0.45	0.288	13.8964	0.0959	−0.0923	−0.1046	
CF		1.95	5.65	3.83	22.47	1.3	3.51	0.78	−8.1	
M1T2	1.87	14.4962	0.0448	−0.286	0.0813	13.5648	0.0287	−0.005	0.043	
CF		4.9	0.90	3.05	3.24	0.56	0.572	0.054	1.74	
M1T9	3.12	13.9135	0.0304	0.150	0.1351	14.2299	0.0167	−0.127	0.0812	
CF		1.10	8.851	5.736	1.914	2.27	4.86	−4.86	1.151	
M1T3	8.11	14.3567	0.1911	0.585	−0.0455	NA	NA	NA	NA	
CF		1.72	5.20	1.715	−4.32					
HRM-2										
M2T1	9.05	NA	NA	NA	NA	14.3879	−0.0193	−0.266	−0.113	
CF						1.74	−1.29	−6.1	1.29	
M2T3	4.33	14.4872	0.0785	0.18	−0.09	14.3836	0.271	−0.067	−0.089	
CF		1.75	1.41	12.81	1.25	1.37	4.87	−4.7	1.21	
M2T4	1.57	14.775	0.281	−0.012	−0.056	14.5025	−0.130	−0.256	−0.041	
CF		4.56	−15.46	0.13	−16.93	2.43	7.14	2.83	−12.60	
M2T6	5.90	14.3358	0.203	0.3	0.13	14.2638	0.09	0.363	0.032	
CF		2.035	3.89	1.6	2.78	1.70	1.74	1.94	0.69	
HRM-3										
M3T1	2.73	14.3087	−0.403	−0.454	0.221	14.517	−0.093	−0.285	0.307	
CF		1.38	2.519	4.266	−17.16	2.30	0.5822	2.678	−23.83	
M3T3	4.68	14.5152	0.051	−0.032	−0.027	14.311	−0.021	0.023	0.0396	
CF		5.03	1.855	−0.793	2.274	3.14	−0.769	0.553	−3.375	
M3T4	3.12	14.3468	0.0583	−0.090	−0.051	13.915	0.014	0.0307	0.0756	
CF		1.60	0.8244	−37.77	5.102	0.59	0.197	12.908	−7.519	
M3T5	6.63	14.2142	0.073	0.104	0.080	14.111	−0.129	0.059	−0.009	
CF		2.17	14.38	6.947	1.714	1.71	−24.35	8.65	1.266	
M3T8	2.73	14.6065	0.2861	0.216	0.139	14.256	0.388	0.0546	−0.079	
CF		3.05	1.2	1.89	3.534	1.38	1.628	0.477	−1.999	

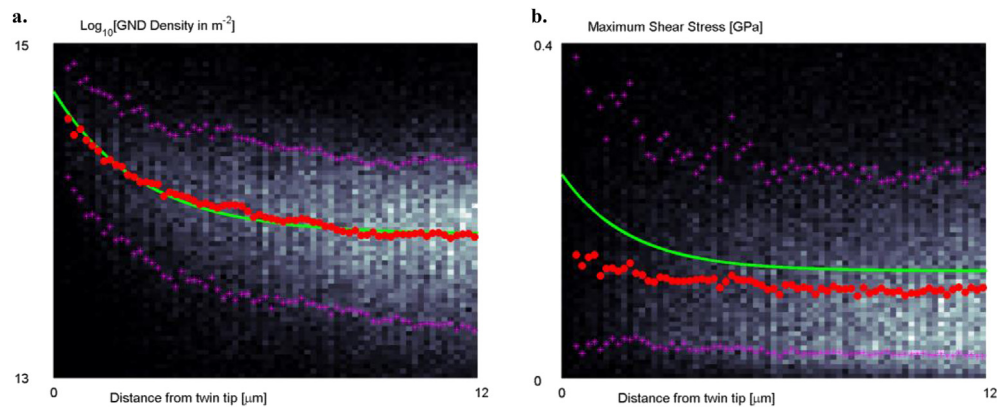


Fig. 8. greyscale indicates frequency of finding given (a) GND density or (b) maximum shear stress at given distance from the twin tip. The red points indicate median, and magenta point 10% and 90% centile values at each distance, while the green line shows the fitting function described in the text. (For interpretation of the references to colour in this figure legend, the reader is referred to the web version of this article.)

maximum in plane shear stress. Fig. 8b shows the frequency at which given maximum shear stress levels were found at different distances from the twin tip, again with 10%, 50% and 90% centile levels shown. In a similar fashion the data can be fit to the form $D + \text{Exp}(-Fx)$ and in this case the value of F indicates a slightly

smaller region of increased stress ($1/F = 1.9 \mu\text{m}$). The distribution of maximum shear stresses is always highly skew with a pronounced tail on the high stress side and this tends to significantly offset the mean and median values so that the functional fit is well above the median values (Fig. 8b).

Table 5Parameters representing the trend in GND density variation close to twin tips in $A + B \exp(-Cx)$ form where x represent distance from the twin tip.

	A	B	C (μm^{-1})
HRM-1	13.67	0.762	0.408
HRM-2	13.89	0.863	0.406
HRM-3	13.84	0.642	0.420
HRM-4	13.66	0.866	0.445

5. Summary

A textured zircaloy-2 sample was uniaxially deformed ex-situ in tension up to 2.7% in a macroscopic direction that favours twin formation. After unloading the sample, the relative stress, elastic lattice rotation, and GND density were measured using the HR-EBSD technique. These parameters were subsequently investigated to understand state of deformation close to twin tips and their

interaction with the surrounding environment. It is shown that:

- 1) There are high concentrations of stress, dislocation density, and lattice rotation close to the twin tip within the parent grain, the immediate neighbouring grain, and within the twin itself.
- 2) It is shown that on average and for the population of the twins and grains that are studied here, maximum GND density and concentration factors happens at the intersection of two twins. Twin tips within twin and twin tips within the neighbouring grain have the second and the third highest values, respectively.
- 3) The state of GND density and stress concentrations within the parent grain changes from one side of the twin boundary to the other side.
- 4) It is shown that the lattice rotation field measured close to the twin boundary is compatible with the twin shear resulted from the variant that caused twinning.
- 5) It is shown that both the GND density and the maximum shear stress increase exponentially close to the twin tips, and are significantly raised within $\sim 2 \mu\text{m}$ of the tip.
- 6) It is shown GND density and concentration factor in the twin neighbouring grain is only a weak function of twin-slip system alignment.

Acknowledgement

The authors would like to acknowledge Prof. Mark Daymond for the provision of material, GATAN and Dr Michael Hassel-Shearer for facilitating and supporting our use of PECS-II. This work is part of the HEXMAT program funded by Engineering and Physical Sciences Research Council (EP/K034332/1). Data in support of this paper will be made accessible on the Oxford Research Archive (www.ora.ox.ac.uk) and on zenodo.org at <http://dx.doi.org/10.5281/zenodo.34597>.

Appendix A. Supplementary data

Supplementary data related to this article can be found at <http://dx.doi.org/10.1016/j.actamat.2015.11.036>.

References

- [1] H. Somekawa, T. Inoue, T. Mukai, Deformation mechanism near crack-tip by finite element analysis and microstructure observation in magnesium alloys, *Mater. Sci. Eng. A* 2010 (1761) 527.
- [2] J. Wang, D. Ju, F. Yin, H. Zhao, Microstructure evaluation and crack initiation crack for AZ31 sheet under biaxial stress, *Procedia Eng.* 10 (2011) 2429.
- [3] P. Müllner, C. Solenthaler, P.J. Uggowitzer, M.O. Speidel, Brittle fracture in austenitic steel, *Acta Metall. Mater.* 42 (1994) 2211.
- [4] M. Koyama, E. Akiyama, K. Tsuzaki, D. Raabe, Hydrogen-assisted failure in a twinning-induced plasticity steel studied under in situ hydrogen charging by electron channeling contrast imaging, *Acta Mater.* 61 (2013) 4607.
- [5] I.A. Ovid'ko, A.G. Sheinerman, Nanoscale cracks at deformation twins stopped by grain boundaries in bulk and thin-film materials with nanocrystalline and ultrafine-grained structures, *J. Phys. D Appl. Phys.* 47 (2014) 015307.
- [6] A. Stoll, A.J. Wilkinson, Simulation of deformation twins and their interactions with cracks, *Comput. Mater. Sci.* 89 (2014) 224.
- [7] C.A. Stein, A. Cerrone, T. Ozturk, S. Lee, P. Kenesei, H. Tucker, R. Pokharel, J. Lind, C. Hefferan, R.M. Suter, A.R. Ingraffea, A.D. Rollett, Fatigue crack initiation, slip localization and twin boundaries in a nickel-based superalloy, *Curr. Opin. Solid State Mater. Sci.* 18 (2014) 244.
- [8] F. Sun, J. Zhang, H. Harada, Deformation twinning and twinning-related fracture in nickel-base single-crystal superalloys during thermomechanical fatigue cycling, *Acta Mater.* 67 (2014) 45.
- [9] F. Sun, S. Zhang, S. Tian, J. Zhang, H. Harada, Large stress concentrations around micropore near a crack-tip induced deformation twinning in Ni-based single crystal superalloy, *J. Alloys Compd.* 586 (2014) 479.
- [10] B. Clausen, C.N. Tomé, D.W. Brown, S.R. Agnew, Reorientation and stress relaxation due to twinning: Modeling and experimental characterization for Mg, *Acta Mater.* 56 (2008) 2456.
- [11] F. Xu, R.A. Holt, M.R. Daymond, R.B. Rogge, E.C. Oliver, Development of internal strains in textured Zircaloy-2 during uni-axial deformation, *Materials Science and Engineering A* 488 (2008) 172.
- [12] O. Muránsky, D.G. Carr, P. Šittner, E.C. Oliver, In situ neutron diffraction investigation of deformation twinning and pseudoelastic-like behaviour of extruded AZ31 magnesium alloy, *Int. J. Plasticity* 25 (2009) 1107.
- [13] C.A. Calhoun, E. Garlea, R.P. Mulay, T.A. Sisker, S.R. Agnew, Investigation of the effect of thermal residual stresses on deformation of α -uranium through neutron diffraction measurements and crystal plasticity modeling, *Acta Mater.* 85 (2015) 168.
- [14] C.C. Aydiner, J.V. Bernier, B. Clausen, U. Lienert, C.N. Tomé, D.W. Brown, Evolution of stress in individual grains and twins in a magnesium alloy aggregate, *Phys. Rev. B* 80 (2009) 024113.
- [15] T. Bieler, L. Wang, A. Beaudoin, P. Kenesei, U. Lienert, In Situ Characterization of Twin Nucleation in Pure Ti Using 3D-XRD, *Metall. Mater. Trans A* 45 (2014) 109.
- [16] H. Abdolvand, M. Majkut, J. Oddershede, S. Schmidt, U. Lienert, B.J. Diak, P.J. Withers, M.R. Daymond, On the deformation twinning of Mg AZ31B: A three-dimensional synchrotron X-ray diffraction experiment and crystal plasticity finite element model, *Int. J. Plasticity* 70 (2015) 77.
- [17] H. Abdolvand, M. Majkut, J. Oddershede, J.P. Wright, M.R. Daymond, Study of 3-D stress development in parent and twin pairs of a hexagonal close-packed polycrystal: Part I – in-situ three-dimensional synchrotron X-ray diffraction measurement, *Acta Mater.* 93 (July 2015) 246–255.
- [18] H. Abdolvand, M. Majkut, J. Oddershede, J.P. Wright, M.R. Daymond, Study of 3-D stress development in parent and twin pairs of a hexagonal close-packed polycrystal: Part II – crystal plasticity finite element modeling, *Acta Mater.* 93 (2015) 235.
- [19] L. Balogh, S.R. Niezgoda, A.K. Kanjarla, D.W. Brown, B. Clausen, W. Liu, C.N. Tomé, Spatially resolved in situ strain measurements from an interior twinned grain in bulk polycrystalline AZ31 alloy, *Acta Mater.* 61 (2013) 3612.
- [20] K.Z. Troost, P. van der Sluis, D.J. Gravesteijn, Microscale elastic-strain determination by backscatter Kikuchi diffraction in the scanning electron microscope, *Appl. Phys. Lett.* 62 (1993) 1110.
- [21] A.J. Wilkinson, Measurement of elastic strains and small lattice rotations using electron back scatter diffraction, *Ultramicroscopy* 62 (1996) 237.
- [22] A.J. Wilkinson, G. Meaden, D.J. Dingley, High-resolution elastic strain measurement from electron backscatter diffraction patterns: New levels of sensitivity, *Ultramicroscopy* 106 (2006) 307.
- [23] T.B. Britton, J. Jiang, R. Clough, E. Tarleton, A.I. Kirkland, A.J. Wilkinson, Assessing the precision of strain measurements using electron backscatter diffraction – part 1: Detector assessment, *Ultramicroscopy* 135 (2013) 126.
- [24] V. Tong, J. Jiang, A.J. Wilkinson, T.B. Britton, The effect of pattern overlap on the accuracy of high resolution electron backscatter diffraction measurements, *Ultramicroscopy* 155 (2015) 62.
- [25] F. Xu, R.A. Holt, M.R. Daymond, R.B. Rogge, E.C. Oliver, Development of internal strains in textured Zircaloy-2 during uni-axial deformation, *Mater. Sci. Eng. A* 488 (2008) 172.
- [26] Abdolvand Hamidreza, Mark R. Daymond, Multi-scale modeling and experimental study of twin inception and propagation in hexagonal close-packed materials using a crystal plasticity finite element approach –Part I: average behavior, *J. Mech. Phys. Solids* 61 (3) (March 2013) 783–802.
- [27] H. Abdolvand, M.R. Daymond, Multi-scale modeling and experimental study of twin inception and propagation in hexagonal close-packed materials using a crystal plasticity finite element approach; part II: Local behavior, *J. Mech. Phys. Solids* 61 (3) (March 2013) 783–802.
- [28] H. Abdolvand, M.R. Daymond, C. Mareau, Incorporation of twinning into a crystal plasticity finite element model: Evolution of lattice strains and texture in Zircaloy-2, *Int. J. Plast.* 27 (2011) 1721.
- [29] S.R. MacEwen, J. Faber Jr., A.P.L. Turner, The use of time-of-flight neutron diffraction to study grain interaction stresses, *Acta Metall.* 31 (1983) 657.
- [30] J. Jiang, T.B. Britton, A.J. Wilkinson, Measurement of geometrically necessary dislocation density with high resolution electron backscatter diffraction: Effects of detector binning and step size, *Ultramicroscopy* 125 (2013) 1.
- [31] J. Jiang, T.B. Britton, A.J. Wilkinson, Evolution of dislocation density distributions in copper during tensile deformation, *Acta Mater.* 61 (2013) 7227.
- [32] T.B. Britton, C. Maurice, R. Fortunier, J.H. Driver, A.P. Day, G. Meaden, D.J. Dingley, K. Mingard, A.J. Wilkinson, Factors affecting the accuracy of high resolution electron backscatter diffraction when using simulated patterns, *Ultramicroscopy* 110 (2010) 1443.
- [33] T.B. Britton, A.J. Wilkinson, High resolution electron backscatter diffraction measurements of elastic strain variations in the presence of larger lattice rotations, *Ultramicroscopy* 114 (2012) 82.
- [34] T.B. Britton, A.J. Wilkinson, High resolution electron backscatter diffraction measurements of elastic strain variations in the presence of larger lattice rotations, *Ultramicroscopy* 114 (2012) 82.
- [35] E.S. Fisher, C.J. Renken, Single-crystal elastic moduli and the HCP–BCC transformation in Ti, Zr, and Hf, *Phys. Rev. B* 135 (1964) 482.
- [36] J.F. Nye, Some geometrical relations in dislocated crystals, *Acta Metall.* 1 (1953) 153.
- [37] T.B. Britton, H. Liang, F.P.E. Dunne, A.J. Wilkinson, The effect of crystal orientation on the indentation response of commercially pure titanium: experiments and simulations, *Proc. R. Soc. A* 466 (2010) 695–719, <http://dx.doi.org/10.1098/rspa.2009.0455>.
- [38] J.J. Jonas, S. Mu, T. Al-Samman, G. Gottstein, L. Jiang, Martin È, The role of strain accommodation during the variant selection of primary twins in magnesium, *Acta Mater.* 59 (2011) 2046.
- [39] X.Y. Zhang, B. Li, X.L. Wu, Y.T. Zhu, Q. Ma, Q. Liu, P.T. Wang, M.F. Horstemeyer,

- Twin boundaries showing very large deviations from the twinning plane, *Scr. Mater.* 67 (2012) 862.
- [40] J.D. Livingston, B. Chalmers, Multiple slip in bicrystal deformation, *Acta Metall.* 5 (1957) 322.
- [41] Z. Shen, R.H. Wagoner, W.A.T. Clark, Dislocation pile-up and grain boundary interactions in 304 stainless steel, *Scr. Metall.* 20 (1986) 921.
- [42] E. Werner, W. Prantl, Slip transfer across grain and phase boundaries, *Acta Metall. Mater.* 38 (1990) 533.
- [43] Y. Guo, D.M. Collins, E. Tarleton, F. Hofmann, J. Tischler, W. Liu, R. Xu, A.J. Wilkinson, T.B. Britton, Measurements of stress fields near a grain boundary: Exploring blocked arrays of dislocations in 3D, *Acta Mater.* 96 (2015) 229.
- [44] T. Zhang, D.M. Collins, F.P.E. Dunne, B.A. Shollock, Crystal plasticity and high-resolution electron backscatter diffraction analysis of full-field polycrystal Ni superalloy strains and rotations under thermal loading, *Acta Mater.* 80 (2014) 25.
- [45] Y. Mikami, K. Oda, M. Kamaya, M. Mochizuki, Effect of reference point selection on microscopic stress measurement using EBSD, *Mater. Sci. Eng. A* 647 (2015) 256.
- [46] C. Mareau, M.R. Daymond, Study of internal strain evolution in Zircaloy-2 using polycrystalline models: Comparison between a rate-dependent and a rate-independent formulation, *Acta Mater.* 58 (2010) 3313.